POLITECNICO DI TORINO
Repository ISTITUZIONALE

In-situ UV cured deep eutectic solvent-based gel polymer electrolyte for Li metal batteries

Original
In-situ UV cured deep eutectic solvent-based gel polymer electrolyte for Li metal batteries / Longo, M., Gandolfo, M., Schimmenti, F., Rodriguez Del Real, J., Meabe, L., Martinez Ibañez, M., Fontana, D., Amici, J.. - In: JOURNAL OF POWER SOURCES. - ISSN 0378-7753. - 674:(2026), pp. 1-11. [10.1016/j.jpowsour.2026.239709]

Availability:
This version is available at: 11583/3008327 since: 2026-03-06T13:45:46Z

Publisher:
Elsevier

Published
DOI:10.1016/j.jpowsour.2026.239709

Terms of use:

This article is made available under terms and conditions as specified in the corresponding bibliographic description in the repository

Publisher copyright

(Article begins on next page)

17 November 2026

Journal of Power Sources 674 (2026) 239709

Contents lists available at ScienceDirect

Journal of Power Sources

journal homepage: www.elsevier.com/locate/jpowsour

In-situ UV cured deep eutectic solvent-based gel polymer electrolyte for Li metal batteries

Mattia Longo [a,*], Matteo Gandolfo [a], Francesco Schimmenti [a], Javier Rodriguez del Real [b], Leire Meabe [b,c], Maria Martinez Ibañez [b], Daniela Fontana [d], Julia Amici [a]

[a] Department of Applied Science and Technology, Politecnico di Torino, C.so Duca degli Abruzzi 24, Torino, 10129, Italy
[b] Centre for Cooperative Research on Alternative Energies, Basque Research and Technology Alliance (BRTA), CIC energiGUNE, Vitoria-Gasteiz, 01510, Spain
[c] Ikerbasque, Basque Foundation for Science, 48013, Bilbao, Spain
[d] COMAU, Grugliasco, 10095, Italy

HIGHLIGHTS

- Non-flammable DES-based gel polymer electrolytes (GPEs) enhance safety and performance in lithium metal batteries (LMBs).
- A scalable in-situ method is demonstrated by UV-curing the electrolyte precursor directly onto the cathode surface.
- Addition of EC and DEC to *g*-DES GPE (*g*-DES10) results in weaker Li^+ coordination and enhanced ionic transport.
- The optimized GPE shows superior interfacial properties with lithium metal.
- Li||LFP cells with *g*-DES10 GPE deliver stable cycling (163 mAh g^{-1}, 113 cycles at 1C), showing suitability for LMBs.

ARTICLE INFO

Keywords:
Lithium metal batteries
Gel polymer electrolytes
Deep eutectic solvents
UV-crosslinking

ABSTRACT

Lithium metal batteries (LMBs) are a promising alternative to obtain high-performance and sustainable energy storage systems, overcoming the energy density limitations of current lithium-ion batteries. However, Li metal hinders their widespread implementation due to high chemical reactivity and dendritic growth, poor interfacial stability and safety concerns linked to the use of flammable liquid electrolytes. Gel polymer electrolytes (GPEs), incorporating non-flammable solvents, have emerged as viable solutions, combining mechanical stability with good electrochemical performance. In this work, a scalable and cheap in-situ fabrication process for a deep eutectic solvent (DES)-based GPE is presented, directly depositing and UV-crosslinking the precursor formulation on the cathode surface. The polyethylene glycol diacrylate-based polymeric matrix is cured in a lithium bis (trifluoromethanesulfonyl)imide (LiTFSI) and trifluoroacetamide (TFA)-based DES, with and without the addition of ethylene carbonate and diethyl carbonate mixture (*g*-DES and *g*-DES10, respectively). Physico-chemical and electrochemical characterizations reveal weaker Li^+ coordination and improved transport properties and favourable interfacial properties in the presence of the carbonates. Li||LFP cells sporting *g*-DES10 GPEs exhibited good interfacial stability and stable cycling (163 mAh g^{-1} over 113 cycles) at room temperature and 1C, demonstrating the suitability of such production processes for scalable, safe and high-performance LMBs.

1. Introduction

As the global demand for renewable energy and electric mobility continues to rise, the inherent limitation of the state-of-the-art electrochemical storage systems, particularly Li ion batteries (LIBs), has become increasingly evident. Although LIBs have been instrumental in enabling the widespread implementation of portable electronics and electric vehicles, their energy density, safety and sustainability are

* Corresponding author.
E-mail addresses: mattia.longo@polito.it (M. Longo), matteo.gandolfo@polito.it (M. Gandolfo), francesco.schimmenti@polito.it (F. Schimmenti), javierrodriguez@cicenergigune.com (J. Rodriguez del Real), lmeabe@cicenergigune.com (L. Meabe), mmartinez@cicenergigune.com (M. Martinez Ibañez), daniela.fontana@comau.com (D. Fontana), julia.amici@polito.it (J. Amici).

https://doi.org/10.1016/j.jpowsour.2026.239709
Received 9 December 2025; Received in revised form 6 February 2026; Accepted 21 February 2026
Available online 28 February 2026
0378-7753/© 2026 The Authors. Published by Elsevier B.V. This is an open access article under the CC BY-NC-ND license (http://creativecommons.org/licenses/by-nc-nd/4.0/).

insufficient to meet the stringent requirements of next-generation applications [1–3]. In this optic, novel and advanced energy storage systems are urgently needed, improving safety, performance and sustainability of the manufacturing process. Li metal batteries (LMBs) are widely regarded as suitable candidates for next-generation energy storage systems and are, thus, being thoroughly investigated due to their potential to overcome LIBs' drawbacks [4–6]. Li metal is considered an ideal anode material due to its extremely high specific capacity of 3860 mAh g^{-1} and low electrochemical reduction potential of −3.04 V *vs* standard hydrogen electrode (SHE) [7]. However, Li metal still presents several notable critical challenges such as its strong reactivity towards water and the formation of unstable solid electrolyte interfaces [8,9]. Moreover, LMBs implementation has been widely associated with limited interfacial stability and uncontrolled dendritic growth leading to compromised cycle life and stability, as well as safety hazards, due to leaking and flammability of conventional liquid electrolytes [10,11].

A promising strategy to address the drawbacks of LMBs is the replacement of the liquid electrolyte with a solid or semi-solid system, avoiding electrolyte leakage and evaporation while mitigating the dendritic formation on the surface of the Li anode [12,13]. Among semi-solid-state electrolytes, gel polymer electrolytes (GPEs) have been widely regarded as suitable and desirable alternatives to liquid-based systems, specifically due to the optimal compromise between their solid-like mechanical stability and their excellent electrochemical properties. Therefore, GPEs can deliver superior electrochemical performances, compared to other solid-state electrolytes, while improving cell safety [14,15]. To further enhance the safety and performance of electrolytes, researchers have focused on emerging non-flammable liquid electrolytes such as ionic liquids and deep eutectic solvents (DESs), as an alternative to conventional carbonate-based liquid systems [16–18]. DESs, typically formed by hydrogen bonds between a hydrogen bond donor (HBD) and a Li salt acting as the hydrogen bond acceptor (HBA), are extremely attractive due to their low volatility, non-flammability, good electrochemical properties and limited environmental impact and are starting to gain attention as possible liquid electrolytes alternatives [19–21]. Li et al. developed an *in-situ* copolymerized self-healing GPE based on pentaerythritol tetraacrylate (PETEA), cystine and 2-isocyanoethyl methacrylate, in combination with a N-methylacetamide (NMA) and lithium bis(trifluoromethanesulfonyl)imide (LiTFSI)-based DES [22]. The mixture was thermally polymerized in a polyethylene separator at 80 °C for 30 min and the assembled Li||lithium iron phosphate (LFP) cells delivered a specific capacity of 135 mAh g^{-1} when cycled at 0.1C. A similar strategy was proposed by Ye et al. where a thiol-ene click reaction was employed to enable the *in-situ* crosslinking of a polymeric matrix composed of polyethylene glycol diacrylate (PEGDA) and pentaerythritol tetrakis (3-mercaptopropionate) (T4) in a DES solution of sulfolane (SL), methyl acrylate (MA), lithium difluoro (oxalato) borate (LiDFOB), 1, 3-diamino-2-propanol (DAP) and LiTFSI [23]. The precursor solution was injected into a supporting cellulose film and reacted for 8 h at room temperature. The resulting Li||LFP cells were cycled at 60 °C for 800 cycles at 1C and presented an initial specific capacity of 164 mAh g^{-1}. Another DES-based GPE was presented by Pei et al., employing a LiTFSI and 1,2-dimethylimidazole (DMIm)-based DES embedded in a polyvinylidene fluoride (PVDF) matrix [24]. The precursor solution was hot-pressed for solvent evaporation and self-standing membranes were obtained. The resulting Li||LFP cells display a high specific capacity of 157 mAh g^{-1} when cycled at 0.1C at room temperature with a good capacity retention. Despite these results, the implementation of DES-based GPEs for LMB applications remains largely under-investigated.

However, in recent years, researchers and engineers are increasingly focusing on designing electrolytes that not only offer high performance but are also economically viable and easily scalable for mass production. In a previous work, a cheap and scalable production process for the *in-situ* preparation of a GPE directly on the cathode surface is reported [25], eliminating the need for a supporting separator and improving the cell energy density by reducing the inactive components content. From a manufacturing perspective, this approach is advantageous as it is fast, easily scalable and reduces the number of processing steps, lowering the overall process cost. Moreover, the *in-situ* deposition results in intimate contact between the precursor formulation and the cathode surface, leading to superior interfacial contact between the crosslinked GPE and the electrode.

Herein, this study proposes a fast, cost-effective, environmentally sustainable, and scalable GPE. Specifically, 1) the GPE is synthesized using a UV-mediated thiol-ene crosslinking reaction, eliminating the need for a separator; 2) it is directly deposited and crosslinked onto the cathode surface; 3) it relies on an DES as the liquid electrolyte medium; and 4) all cell assembly processes are conducted in a controlled dry environment. The development and characterization of the PEGDA and T4-based GPE is reported, employing a LiTFSI and trifluoroacetamide (TFA)-based DES as the liquid electrolyte medium (referred to as *l*-DES). Although TFA has received limited attention in the context of DESs, preliminary studies have shown interesting properties and good stability against lithium metal [26]. The addition of 10 *wt*% of an EC/DEC solution (1:1 *wt* ratio, referred to as EDL in the text) in the *l*-DES was investigated (referred to as *l*-DES10), with the aim of further optimizing the electrochemical performances during operation by reducing the DES viscosity. The physico-chemical properties and the electrochemical performances of the liquid DES-based electrolytes were thoroughly investigated, focusing on the evaluation of Li^{+} coordination and chemical environment in the liquid *l*-DES and *l*-DES10, as well as in the GPE precursor formulations. As a result, the cycling performances of the obtained GPEs was investigated at 25 °C in a Li||LFP cell at 1C. The combined approach of DES-based GPE design and *in-situ* GPE preparation represents a comprehensive strategy toward safer and high-performance LMBs.

2. Experimental

2.1. Materials

PEGDA (M_n = 575 g mol^{-1}), T4, TFA, 2,2-dimethoxy-2-phenylacetophenone (DMPA), ethylene carbonate (EC), diethyl carbonate (DEC), LiTFSI, 1-metil-2-pirrolidone (NMP) and PVDF (8% solution in NMP) were obtained from Sigma-Aldrich and used without further purification. LFP (800 μm particle size) and carbon black (C65) were purchased from Aleees and Imerys Graphite & Carbon, respectively.

2.2. DES preparation

The DES solution was prepared by mixing LiTFSI and TFA with a molar ratio of 1:4 for 2 h at 50 °C in an Ar-filled glovebox (Mbraun Labstar, Stratham, NH, USA, O_2 and H_2O contents <0.5 ppm).

2.3. GPE preparation

The precursor solution was prepared by mixing PEGDA and T4 (thiol: vinyl = 1:1 M ratio) in a dry atmosphere (10% relative humidity, dew point −60 °C). 90 *wt*% of DES solution was added to obtain the *g*-DES precursor solution (90:10 *wt*% liquid:polymer ratio). In the case of the *g*-DES10 precursor solution, 10 *wt*% of EDL was further added with respect to the liquid weight (maintaining the 90:10 *wt*% liquid:polymer ratio). In all cases, 2 *wt*% of DMPA photoinitiator, with respect to the polymer weight, was added, and 250 μL of precursor solution was directly deposited on the LFP cathode surface and irradiated with a UV lamp (10 W, 365 nm, DARKDAWN, China) for 6 min until completely crosslinked.

2.4. LFP cathode production

To prepare the cathode, a slurry containing 70 *wt*% LFP, 20 *wt*% C65

and 10 *wt%* PVDF in NMP was cast onto an aluminium foil and dried in a vacuum oven at 70 °C for 12 h. The calendering process was carried out via a hot rolling press (MSK-HRP-01, MTI Group, Richmond, United States) at 90 °C obtaining a cathode layer thickness reduction of 30%. Disks with a 12 mm diameter were cut and further dried in vacuum oven at 120 °C for 6 h. The active material mass loading of the obtained cathodes was ≈2 mg cm^{-2}.

2.5. Cell assembly

The cell assembly was carried out in the dry room (dew point −60 °C) with lithium chips (15.6 mm × 0.62 mm, Chemetall s.r.l., Giussano, Italy) employed as the anode. Li|GPE|LFP full cells were assembled in ECC-Std (EL-Cell, GmbH, Hamburg, Germany) type cells.

2.6. Physico-chemical characterization

The chemical environment in the precursor solutions was investigated via NMR analysis employing a Bruker 300 MHz spectrometer. The donor number (DN) of TFA was computed from the ^{23}Na NMR spectrum of a 0.1 M solution of sodium bis(trifluoromethanesulfonyl)imide (NaTFSI) in melted TFA, employing a 3 M solution of sodium chloride (NaCl) in deuterated water (D_2O) as a reference. The test was carried out at 80 °C and the value of DN was estimated from Eq. (1) [27,28].

$$DN = 2.106 \cdot {}^{23}\delta + 32.74 \quad (1)$$

Infrared spectra were collected by Attenuated Total Reflectance Fourier-Transform Infrared (ATR-FTIR) technique using a Vertex-70 Bruker spectrometer. The spectra were collected in the 4000-400 cm^{-1} spectral range with an average of 64 scans and a resolution of 4 cm^{-1}. Raman spectroscopy was carried out on the samples in a Renishaw inVia confocal Raman spectrometer, employing a 532 nm incident laser wavelength and a 3600-100 cm^{-1} Raman shift range. Both FTIR and Raman spectra were fitted with Origin software employing the Gaussian function. The thermal properties of the liquid ES-based solutions and the crosslinked GPEs were evaluated via Netzsch DSC 204 F1 calorimeter (Selb, Germany) between −80 and 60 °C with a scan rate of 10 °C min^{-1} in an inert N_2 atmosphere, while the thermal resistance of the oligomers and the membranes was explored by means of a thermogravimetric analysis (TGA) with a Netzsch thermo-microbalance (TG 209 F3 Tarsus, Selb, Germany) between 30 and 800 °C in N_2 with a rate of 20 °C min^{-1}. The polymerization kinetics was studied by monitoring the storage modulus of the cured gels with an Anton PAAR Modular Compact Rheometer (Physica MCR 302, Graz, Austria) sporting a quartz bottom glass during UV irradiation with a Hamamatsu UV LightningCure LC8 L9588 UV lamp. The gel time was computed as the time for which the storage modulus G′ surpasses the loss modulus G''. The viscosity of the liquid electrolytes was evaluated at 40 °C while the test for the precursor formulations was carried out at 25 °C. Mechanical compression testing was performed by an MTS Systems Corporation dynamometer (MTS QTestTM/10 Elite, Eden Prairie, MN, USA) with a 10 N load cell and a 1 mm min^{-1} compression rate. The compression modulus was computed as the slope of the initial elastic region.

2.7. Electrochemical characterization

Electrochemical impedance spectroscopy (EIS) was employed to calculate the ionic conductivity of the membranes. The EIS measurements were performed by a VSP3-e multichannel potentiostat (Biologic, Seyssinet-Pariset, France) in the frequency range between 1 Hz and 10^5 Hz at open circuit voltage (OCV) with an amplitude of 0.01 V. The measurements were carried out in the temperature range between 20 and 60 °C in a dynamic climatic chamber (BINDER GmbH, Tuttlingen, Germany) employing a stainless-steel SS|GPE|SS symmetrical cell configuration (ECC-Std, EL-Cell, GmbH, Hamburg, Germany). The values of the ionic conductivities were computed by Eq. (2).

$$\sigma = \frac{s}{(R_b \cdot A)} \quad (2)$$

where σ is the ionic conductivity, s and A are respectively the GPE thickness and area and R_b is the bulk resistance of the membranes computed from the intercept of the high-frequency Nyquist plot of the EIS measurement. The long-term interfacial stability of the GPEs in contact with Li metal at room temperature was investigated by EIS measurements performed daily for a month in symmetrical Li|GPE|Li cells. The Li^+ transference number (T_{Li^+}) of the GPEs was computed from EIS measurements performed before and after a chronoamperometry (CA, 10 mV) on a symmetrical Li|GPE|Li cell, as described by Bruce and Vincent with Eq. (3) [29]:

$$T_{Li^+} = \frac{I_s \cdot (\Delta V - I_0 R_0)}{I_0 \cdot (\Delta V - I_s R_s)} \quad (3)$$

where I_s and I_0 are the steady state and initial currents, R_s and R_0 are the steady state and initial interfacial resistances and ΔV is the applied voltage. The electrochemical stability of the GPE was investigated by linear sweep voltammetry (LSV) performed on SS|GPE|Li half cells in the voltage range between 2 and 5 V *vs* Li/Li^+ with a scan rate of 0.1 mV s^{-1} employing a CHI660D Electrochemical Workstation (CH Instruments, Inc, Austin, TX, USA). A BT-2000 battery tester (Arbin Instruments, College Station, USA) was employed to carry out the plating and stripping tests on symmetrical Li|GPE|Li cells with a current density of 0.1 mA cm^{-2} and a limited capacity of 0.1 mAh cm^{-2}. The same battery tester way employed to perform the critical current density (CCD) test, increasing the current density from 0.05 mA cm^{-2} to 1 mA cm^{-2} retaining a step time of 1 h on symmetrical Li|GPE|Li cells. The galvanostatic cycling of Li||LFP cells was carried out in a VMP3-e multichannel potentiostat (Biologic), between 2.5 V and 3.8 V, with a current density of 1C and a constant voltage step after each charge step. The temperature during cycling was controlled with a BINDER KB23 Cooling incubator and kept at 25 °C.

3. Results and discussion

3.1. Physico-chemical characterization

The deep eutectic solvent (*l*-DES) employed for GPEs preparation was prepared by mixing TFA and LiTFSI crystals in a 4:1 M ratio, as reported in literature [26]. The ratio 4:1 was chosen as it results in the highest ionic conductivity, reported in Fig. S1. Nonetheless, the presence of several broad crystallization and melting peaks in the temperature range between −20 °C and 35 °C are observed by DSC analysis, Fig. S2, indicates the presence of a dual-phase region where both solid and liquid species are present in a 4:1 M ratio. This phenomenon is a clear indication that the ratio of 4:1 is not, in fact, the eutectic composition of the TFA/LiTFSI based DES [30]. From the DSC spectrum of the *l*-DES, it is possible to evaluate the *solidus* temperature T_S, defined as the temperature at which the mixture begins to solidify, as −7 °C and the *liquidus* temperature T_L, defined as the temperature at which the last solid specie melts, as 32 °C. The addition of 10% *wt* of a 1:1 mixture of EC/DEC (*l*-DES10, also reported in Fig. S2) causes the T_S and the T_L of the formulation to shift at lower temperatures, namely −29 °C and 28 °C respectively, due to the increase in the configurational entropy of the mixture [31]. The detected temperature shift enables a fully liquid DES existence in a broader temperature range. The EDL addition, moreover, reduces the viscosity of the liquid DES and, consequently, leads to higher ionic conductivity (shown in Fig.S3 and Fig.S1, respectively). The thermal stability of both formulations was investigated by means of TGA analysis. From the thermograms reported in Fig. S4, an almost identical onset temperature of weight loss (identified as the temperature at which the weight loss reaches 2%) was measured, namely 74 °C and 75 °C.

From the thermograms, two weight loss steps, with the maximum rate temperatures recorded at around 130 °C and 420 °C, are identified and assigned to the TFA and LiTFSI degradation, respectively [32,33].

The strong interaction between TFA and Li^+ has been reported through molecular dynamics studies, with the carbonyl oxygen atom of the acetamide closest to the Li^+, forming the eutectic solution [34] and favouring Li^+ transport properties [26]. In this context, to evaluate the coordination environments of the species, the DN value of TFA was determined. ^{23}Na NMR was employed to evaluate the DN of the TFA via Eq. (1) which was found to be equal to 18.63 kcal mol^{-1} (Fig. S5). Such a high value of DN is instrumental in enabling the LiTFSI salt dissociation and the strong solvation of the Li^+ in the DES by TFA. To confirm these assumptions, the interactions between the species in TFA and in the *l*-DES were evaluated by means of FTIR. Fig.S6.a displays the TFA and *l*-DES FTIR spectra inserts in the 1550-1900 cm^{-1} wavenumber range (the full FTIR spectra of TFA and *l*-DES are reported in Fig.S6.b). In the TFA FTIR spectrum, the most intense peak, centred around 1706 cm^{-1}, was assigned to the free C=O stretching vibration while the smaller peak at 1641 cm^{-1} was associated to the stretching vibration of the negatively charged C=O interacting via H-bond with the positively charged NH_2 group forming a dimer [35–37], as illustrated in Fig.S6.c. With the addition of LiTFSI in the system and the generation of the eutectic solution, the dimer peak disappears, and another peak arises at 1610 cm^{-1}, associated with the C=O—Li^+ coordination [38–41]. Once EDL is combined with *l*-DES, the Li^+ chemical environment and its solvation structure are studied by ^{7}Li, ^{1}H and ^{19}F NMR, FTIR and Raman spectroscopy (Fig. 1.a-e). Although EC and DEC present smaller DN values (16.4 kcal mol^{-1} and 16 kcal mol^{-1}, respectively [42,43]), it is important to consider that their addition in the *l*-DES leads to an increase in the C=O molar concentration.

The upfield shift of the ^{7}Li signal for the *l*-DES10 sample, observed after the EDL addition, can be associated with an increase in the shielding around the Li^+ nucleus (Fig. 1.a). This result is counterintuitive as the addition of co-solvents has been reported to increase the configurational entropy of the solvation shell and thus weaken the coordination of the cations [31]. However, it is the authors' hypothesis that the increase in the C=O molar concentration could compensate for the increase in configurational entropy and result in a slightly stronger C=O—Li^+ coordination [44].

Concurrently, the downfield shift of the ^{1}H and the ^{19}F peaks (Fig. 1. b and c), related to the NH_2 and the CF_3 groups of the TFA, respectively, can be caused by the increase in the number of TFA—TFA H bonds, as

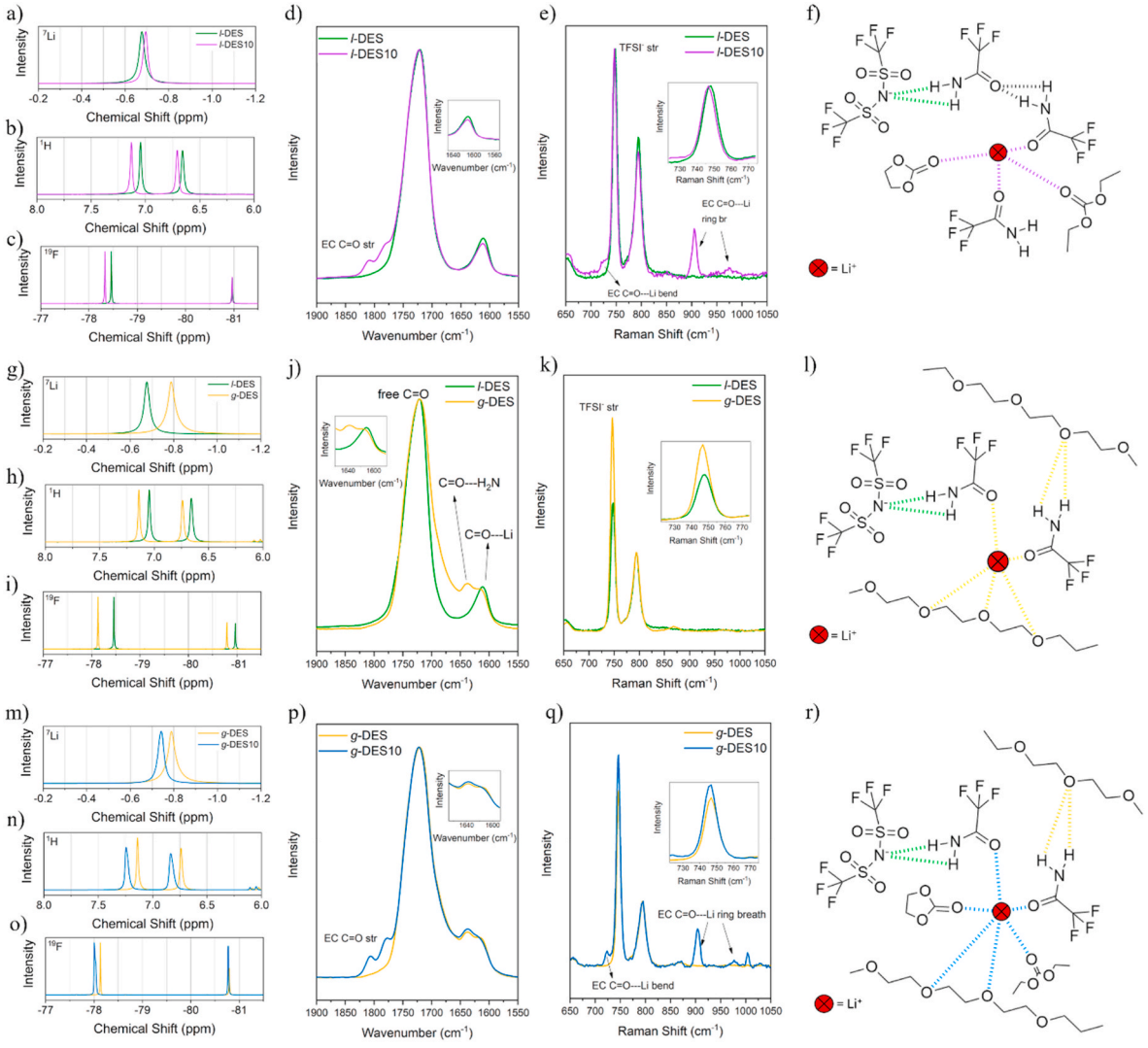


Fig. 1. (a) ^{7}Li NMR, (b) ^{1}H NMR, (c) ^{19}F NMR (d) FTIR and (e) Raman spectra comparison between *l*-DES and *l*-DES10. (f) Schematic representation of *l*-DES10 interactions. (g) ^{7}Li NMR, (h) ^{1}H NMR, (i) ^{19}F NMR (j) FTIR and (k) Raman spectra comparison between *l*-DES and *g*-DES. (f) Schematic representation of *g*-DES interactions. (m) ^{7}Li NMR, (n) ^{1}H NMR, (o) ^{19}F NMR (p) FTIR and (q) Raman spectra comparison between *g*-DES and *g*-DES10. (r) Schematic representation of *g*-DES10 interactions.

well as possible interactions between the C=O groups of EC and DEC and the positively charged NH_2 groups. On the other hand, the increase in Li nucleus shielding with EDL addition still results in a less shielded Li nucleus with respect to a 1 M LiTFSI in EC/DEC (a standard electrolyte), as shown in Fig. S7, which may indicate a more dynamic solvation shell. In the FTIR plot, reported in Fig. 1.d, the addition of EDL results in the appearance of two bands at 1809 cm^{-1} and 1780 cm^{-1}, associated with the C=O stretching of EC and the associated Fermi resonance [45–47]. It is reported that the DEC carbonyl stretching is centred around 1740 cm^{-1} and thus, it is not visible due to overlap with the TFA carbonyl peak [46]. Besides, the decreased intensity of the 1610 cm^{-1} vibration could stem from the weaker TFA—Li^+ interaction due to the establishment of the EDL—Li^+ interactions. Another confirmation of the presence of interactions between the carbonates and Li^+ can be given considering the presence of the 725 cm^{-1}, 905 cm^{-1} and 975 cm^{-1} in the Raman spectra, related to C=O bending and ring breathing of the EC structure when coordinating with a cation [48], as well as the slight redshift of the 745 cm^{-1} peak, associated with the expansion and contraction of $TFSI^-$ suggests a higher degree of dissociation, as reported in the insert of Fig. 1.e (full Raman spectra reported in Fig. S8) [49–51]. All in all, a simplified schematic of the chemical interactions in the *l*-DES10 electrolyte is reported in Fig. 1.f, where the competition between the solvation of the Li^+ by the TFA and the carbonates is illustrated. Next, the impact of polymer presence on the coordination environment is evaluated. Considering the interactions between the *l*-DES and the oligomers chains in the *g*-DES precursor formulation, a significant upfield shift is recorded in the ^{7}Li NMR spectrum reported in Fig. 1.g. The increase in Li nucleus shielding stems from the stronger coordination of Li^+ to the ethylene oxide (EO) segments in the PEGDA chains, which display a DN of 20 kcal mol^{-1} [52]. The greater occurrence of TFA—TFA interactions, through H-bonding, is further confirmed by the downfield shift of the ^{1}H and ^{19}F peaks related to the TFA in the spectra reported in Fig. 1.h and i. Interestingly, the ^{19}F signal relative to the $TFSI^-$ anion around −80.7 ppm in the *g*-DES formulation displays a downfield shift compared to the *l*-DES and *l*-DES10 spectra. Considering the $TFSI^-$ charge delocalization, the deshielding of the F atoms could be caused by the weaker interactions of the $TFSI^-$ anion with the Li^+ [53]. The appearance of the H-bond peak at 1641 cm^{-1}, in the FTIR spectra, and the decrease in intensity of the C=O—Li^+ stretching peak of the TFA at 1610 cm^{-1} in Fig. 1.j can both be attributed to the stronger interactions between Li^+ and the EO units of the PEGDA (with the full FTIR spectra reported in Fig. S9). Additionally, a slight redshift of both the Raman peak associated to the CF_3 stretching from 1247 cm^{-1} in the *l*-DES to 1245 cm^{-1} in the *g*-DES formulation (Fig. S10) and the Raman peak associated to the S−N−S stretching from 748 cm^{-1} in the *l*-DES to 746 cm^{-1} in the *g*-DES are measured (Fig. 1.k) (full Raman spectra of *g*-DES and *g*-DES10 in Fig. S11). The shifts of the $TFSI^-$ signals in the Raman spectra could also be associated with a stronger dissociation of the LiTFSI salt due to the strong coordination of the Li^+ with the EO segments in the polymeric matrix [54,55], schematically displayed in Fig. 1.l. On the other hand, the *g*-DES10 precursor formulation displays a much more dynamic chemical environment in the Li^+ solvation shell. The weaker Li^+ solvation in the *g*-DES10 linked to the more disordered Li^+ solvation environment results in the downfield shift of the Li^+ peak in the ^{7}Li NMR spectrum of *g*-DES10 with respect to the *g*-DES (Fig. 1.m). The strong solvation of Li^+ by the EO units of the polymer chains, exemplified by the greater DN of PEGDA, competes with the comparatively weaker solvation of Li^+ in the *l*-DES10 liquid phase. Comparing the ^{7}Li shift of the *g*-DES10 formulation with a reference (*g*-1 M LiTFSI in EC/DEC containing PEGDA and T4), it is clear that the DES-based GPE precursor formulation displays much more deshielded Li nuclei, which indicates stronger Li coordination in the *g*-1 M LiTFSI in EC/DEC sample (Fig. S12). The greater extent of TFA—TFA interactions is further confirmed by the greater downfield shift of the ^{1}H and ^{19}F NMR peaks in Fig. 1.n and o, caused by the substitution of some TFA molecules in the Li^+ solvation shell with EC and DEC molecules. The addition of the EDL mixture, again, causes a slight decrease in the intensity of the C=O—Li^+ of the TFA at 1610 cm^{-1} in the FTIR spectra with the consequential increase in the intensity of the H-bond peak of the TFA at 1641 cm^{-1}, reported in Fig. 1.p. The decrease in the Li nucleus shielding upon EDL addition is possibly caused by the lower viscosity of the liquid phase and the increase in the C=O molar concentration. The increased dissociation of LiTFSI is demonstrated by the slight redshift of the Raman peak related to $TFSI^-$ from 746 cm^{-1} to 745 cm^{-1}, reported in Fig. 1.q. Moreover, the appearance of Raman peaks at 725 cm^{-1}, 905 cm^{-1} and 975 cm^{-1} in Fig. 1.q can be again regarded as proof of the carbonate interactions with Li^+ [48], with the schematized Li^+ interactions reported in Fig. 1.r.

To evaluate possible differences in the thermal behaviour of the formulations after the mixing of the DES-based liquid electrolyte with the polymeric precursors, DSC tests were carried out. The measured DSC spectra for the precursor solutions and the crosslinked GPEs are reported in Fig. 2.a and confirm the presence of several thermal transitions in the temperature range between −40 °C and 40 °C. The *g*-DES10 formulation, both before and after the crosslinking reaction, displays slightly lower T_L with respect to the *g*-DES one. Before crosslinking, the T_L shifts from 35 °C for *g*-DES to 32 °C for *g*-DES10, while after UV-curing, the T_S drops from 35 °C for *g*-DES to 26 °C for *g*-DES10, allowing the DES to remain liquid at room temperature inside the crosslinked polymer matrix. Furthermore, the lower viscosity of *g*-DES10 precursor formulations, reported in Fig. 2.b, is attributed to the addition of the low viscosity EDL solution, as well as the increase in configurational entropy of the solvation shell [31]. This reduction is further confirmed by monitoring the loss (G'') moduli of *g*-DES and *g*-DES10 during the crosslinking reactions, reported in Fig. 2.c, which highlights the lower viscosity of the *g*-DES10 formulation. This decrease in viscosity could also contribute to the shorter gel time, defined as the time for which G'>G'' in the case of a crosslinking solution, which drops from 12 s for the *g*-DES to 8 s for the *g*-DES10 [56].

Moreover, considering the G′ values measured for both GPEs at the end of the crosslinking reactions, it is possible to evaluate a significant decrease from 45.2 kPa for the *g*-DES to 19.2 kPa for the *g*-DES10. Such a decrease in G′ is possibly caused by the weaker interactions between the oligomer chains and the liquid phase after the EDL addition. The weaker interactions lead to more contracted chains and thus, to a slower crosslinking reaction [57,58]. Moreover, it is reported that metal cations can act as temporary crosslinkers in gels, increasing the crosslinking density and thus the storage modulus G'. The decrease in G' measured after the addition of the EDL solution could result from the increase in Li^+ mobility in the liquid phase [59,60]. This trend is further confirmed by the compression test (Fig. S13) with a slight reduction in compression modulus values of the crosslinked GPEs from 21.01 ± 0.28 kPa for the *g*-DES to 19.83 ± 0.55 kPa for the *g*-DES10.

Lastly, the superior safety of the DES-based GPEs was evaluated via flammability test. For comparison, a control membrane was obtained by crosslinking the oligomers in the carbonate liquid electrolyte (*g*-1 M LiTFSI in EC/DEC). As shown in Fig. 2.d, both *g*-DES and *g*-DES10 present a complete resistance to ignition and fire, even after two consecutive 10 s ignitions, and therefore, both membranes can be considered significantly safer than the highly flammable control GPE. These results confirm the non-flammability and the superior safety of the DES-based GPEs, advantageous for practical applications of solid-state LMBs.

3.2. Electrochemical characterization

The ionic conductivity of the GPEs was computed via Eq. (2) based on PEIS measurements in the temperature range from 20 °C to 60 °C. Self-standing membranes were prepared in dry room by crosslinking the precursor formulation on a glass substrate. As reported in Fig. 3.a, the test confirms the higher ionic conductivity of the *g*-DES10 compared to *g*-DES throughout the whole temperature range, with conductivity values at 20 °C of 1.25 × 10^{-3} S cm^{-1} and 6.36 × 10^{-4} S cm^{-1},

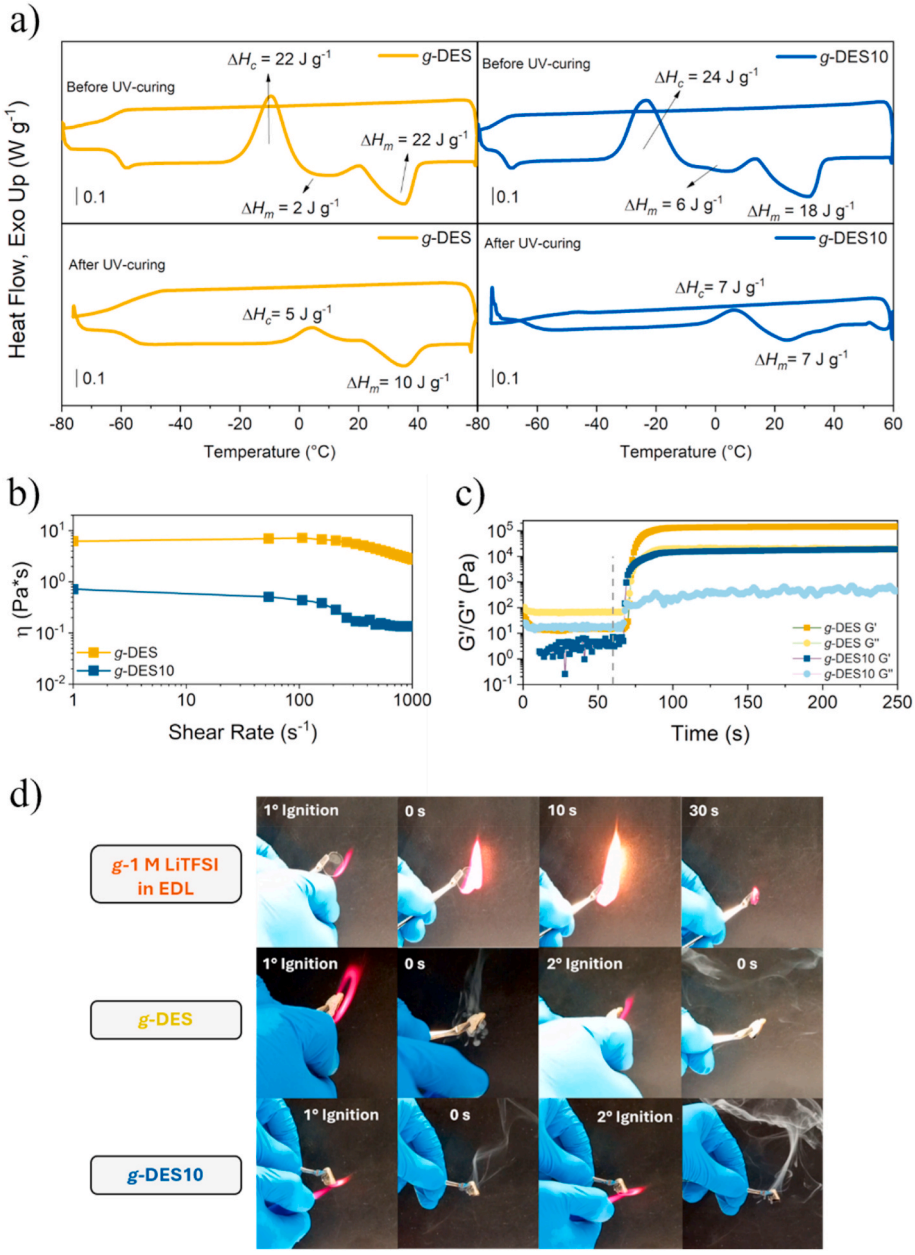


Fig. 2. (a) DSC curves of *g*-DES and *g*-DES10 before and after UV-curing. (b) Comparison between *g*-DES and *g*-DES10 solutions viscosity before UV-curing. (c) Photorheometric curves of *g*-DES and *g*-DES10 during UV irradiation. (d) Flammability tests of *g*-1 M LiTFSI in EDL, *g*-DES and *g*-DES10.

respectively.

The significative increase in ionic conductivity can be correlated with the decrease in liquid phase viscosity, as well as the weaker coordination of the Li^+, as confirmed by NMR and spectroscopic analysis. Additionally, to further understand the ion transport efficiency within the polymer matrix, the Li^+ transference number T_{Li^+} was evaluated for both formulations using Eq (3). As reported in Fig. 3.b and Fig. S14, the *g*-DES sample displays a T_{Li^+} of 0.65 while the carbonates addition leads to a comparable value of T_{Li^+} of 0.67. Such high values of T_{Li^+} are extremely advantageous during cell operation as they reduce cell polarization and interfacial resistance, leading to more homogeneous Li plating and stripping. The total conductivity, T_{Li^+} and Li^+ conductivity, reported in Fig. 3.b, further confirm that the addition of the EDL solution significantly improves the Li^+ transport properties, with the Li^+ conductivity increasing from 4.13×10^{-4} S cm^{-1} for *g*-DES to 8.37×10^{-4} S cm^{-1} for *g*-DES10 at 20 °C.

In order to evaluate the interfacial stability of the crosslinked GPEs in contact with Li metal, symmetric Li|GPE|Li cells containing both *g*-DES and *g*-DES10 membranes were kept at open circuit voltage (OCV) for one month, performing PEIS measurements daily. The evolution of the Nyquist plots for both cells in the considered period is reported in Fig. S15 and summarized in Fig. 3.c. Interestingly, the charge transfer resistance (R_{ct}) values of the investigated cells display opposite trends during the interfacial stability test. The *g*-DES cell presents an increase in the values of R_{ct} from the initial 147 Ω cm^2 to 198 Ω cm^2 after 30 days at OCV, suggesting continuous side reactions between Li metal and TFA at the interface over time, possibly caused by the generation of a porous and unstable interfacial layer. On the contrary, the *g*-DES10 cell displays a sharp decrease in R_{ct} after the first 10 days of testing, from 171 Ω cm^2 to 103 Ω cm^2, and reaches 99 Ω cm^2 after 30 days. Interestingly, the EDL addition in the liquid phase of the gel in contact with Li metal has not resulted in a decrease in interfacial stability [25,61]. The R_{ct} evolution can be regarded as proof of the generation of a stable interface after the prolonged contact of the *g*-DES10 membrane with Li metal and as a

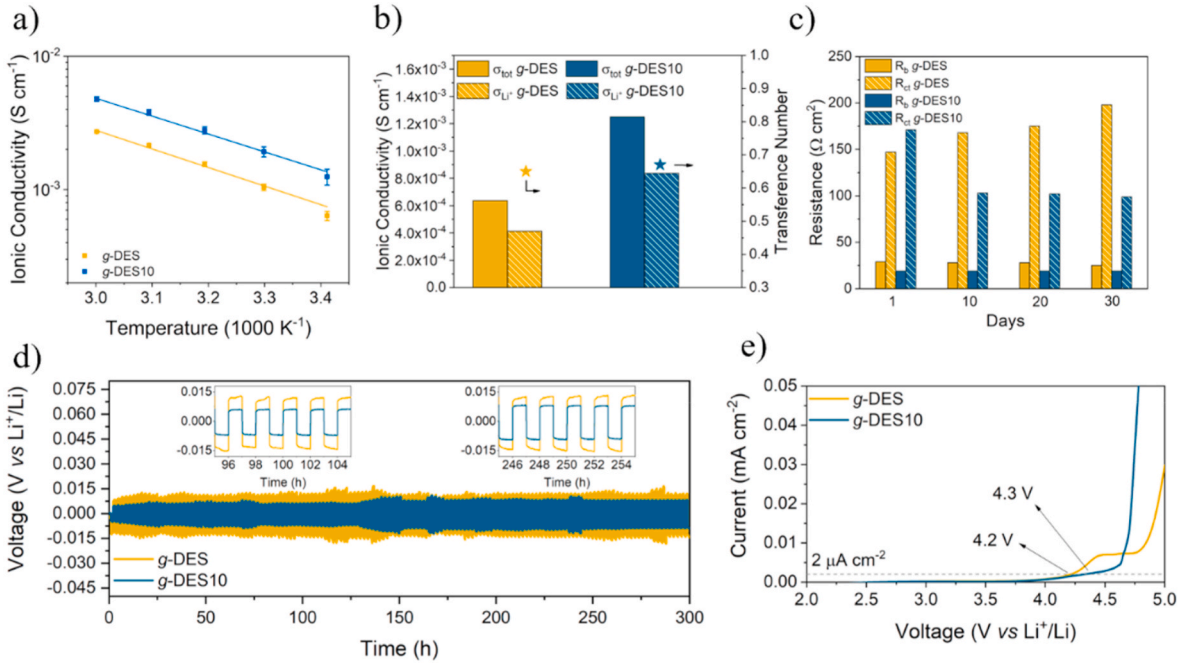


Fig. 3. (a) Dependence of ionic conductivity of *g*-DES and *g*-DES10 on temperature. (b) Room temperature ionic conductivity, Li^+ conductivity and transference number of *g*-DES and *g*-DES10. (c) Bulk and charge-transfer resistance evolution for *g*-DES and *g*-DES10 in symmetric Li||Li cells. (d) Stripping and plating profiles and (e) LSV curves of *g*-DES and *g*-DES10.

confirmation of the stability of such GPE with Li metal in static conditions. To evaluate the practical impact of the improved transport properties, the deposition and dissolution of Li were evaluated in a symmetrical Li|GPE|Li cell, employing self-standing membranes prepared in a dry room. The galvanostatic plating and stripping test was carried out at 25 °C with a current density of 0.1 mA cm^{-2} and a limited capacity of 0.1 mAh cm^{-2}. Both *g*-DES and *g*-DES10 cells displayed low and constant overpotentials during the plating and stripping test, shown in Fig. 3.d, with final values of 12.1 mV *vs* Li^+/Li and 8.2 mV *vs* Li^+/Li, respectively, further confirming the generation of a more conductive interface for *g*-DES10. Another confirmation of the beneficial effect of the EDL addition to the DES-based electrolyte is the increase in the CCD, as reported in Fig. S16, from 0.5 mA cm^{-2} for *g*-DES to 1 mA cm^{-2} for *g*-DES10. The flatter voltage profile, lower cell polarization and superior CCD demonstrated by the *g*-DES10 formulation can be linked to the superior Li-ion conductivity and more conductive Li/electrolyte interface presenting lower R_{ct} obtained after the EDL addition [62]. To further evaluate the voltage stability of the GPEs, a LSV test was conducted on SS|GPE|Li cells. As reported in Fig. 3.e, both *g*-DES and *g*-DES10 formulations exhibit comparable electrochemical stability. The limited electrochemical stability windows (ESWs), namely 4.2 V and 4.3 V for *g*-DES and *g*-DES10, respectively, were related to the high HBD concentration, which may undergo oxidative degradation at higher potentials [63,64]. Nevertheless, the slightly broader ESW displayed by *g*-DES10 is in line with the general improvement in the electrochemical stability upon EDL addition [65,66].

3.3. Galvanostatic cycling

To assess the impact of the addition of the carbonates solution in the GPEs, galvanostatic cycling of cells were conducted on Li|GPE|LFP cells, reported in Fig. 4.a. The cells were cycled with a current density of 1C between 2.5 V and 3.8 V, employing a constant voltage step after each charge process and measuring the PEIS every cycle for the first 20 cycles and each 10 cycles thereafter. The improvement in ionic conductivity and transport properties associated with the increase in entropy of the Li^+ solvation shell is demonstrated by the significant increase in specific capacity values, cycling stability and cell lifetime.

The *g*-DES-based cell and, to a lesser extent, the *g*-DES10 cell display an initial increase in specific capacity during the first five cycles, likely due to the activation of the Li/GPE interfaces. The *g*-DES cell presents a specific capacity peak value of 125 mAh g^{-1}, after which the capacity fades rapidly and constantly. This can be possibly linked to the accumulation of degradation products at the Li interface, increasing the interfacial resistance and promoting cell polarization. The *g*-DES10-based cell, on the other hand, displays stable cycling, with a specific capacity of 163 mAh g^{-1} retained for 113 cycles. The improvement in electrochemical performance is additionally supported by the PEIS data, reported in Fig. 4.b and c and summarized in Fig. 4.d, reporting the fitted resistance values during cycling. The initial R_{ct} value for the *g*-DES10 cell was measured at 175 Ω cm^2, significantly lower than the 326 Ω cm^2 measured for the *g*-DES one. Furthermore, the *g*-DES10 cell presents a more gradual increase in R_{ct} values during cycling, reaching 278 Ω cm^2 after 40 cycles, as opposed to the 964 Ω cm^2 of the *g*-DES cell. After 120 cycles, the R_{ct} of the *g*-DES10 cell increases to 707 Ω cm^2, highlighting the superior interfacial stability obtained after the 10 *wt%* carbonates addition. The all-around improvements in ionic conductivity, Li^+ transport properties and interfacial stability contribute to the lower cell polarization evaluated for the *g*-DES10 cell, reported in Fig. 4.e. To better understand the source of the difference in performances and the interfacial properties of the considered samples, a *post-mortem* investigation of the Li-electrolyte interface was carried out. Li|LE|LFP cells were assembled in an Ar-filled glovebox to assess the performances of the two liquid electrolytes, *l*-DES and *l*-DES10. The morphology of the Li anode of cells containing the GPEs was not evaluated as it was not possible to retrieve Li anodes without modifying the Li surface morphology. The assembled cells were tested by galvanostatic cycling for 60 cycles at a current density of 1C at 25 °C and the cycled Li anodes were retrieved to evaluate lithium morphology by SEM. The specific capacity evolution plots are reported in Fig. 5.a and b, displaying stable cycling.

Fig. 5.c and d display micrographs of the anode surface from both cells after cycling in the charged state. *l*-DES10 based electrolytes clearly reports a smoother and more homogeneous Li anode surface, in line with

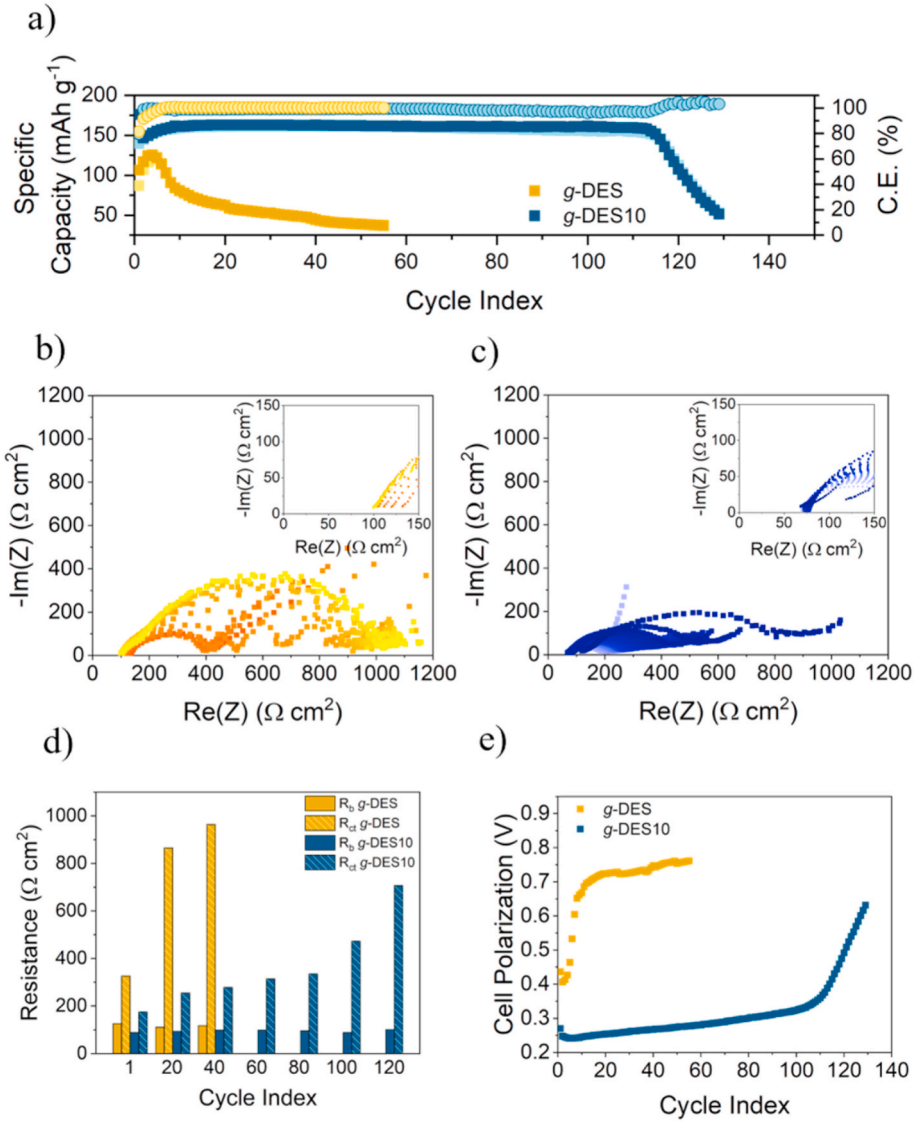


Fig. 4. (a) Specific capacity and Coulombic efficiency of *g*-DES and *g*-DES10 during galvanostatic cycling. EIS spectra evolution of (b) *g*-DES and (c) *g*-DES10. (d) Bulk and charge-transfer resistance and (e) Cell polarization evolution for *g*-DES and *g*-DES10 in Li||LFP half cells.

the superior interfacial properties. This morphology suggests a more controlled and homogeneous lithium plating process, attributed to the improved transport properties of the DES-based liquid electrolyte upon EDL addition. The anode surface of the *l*-DES cell, on the other hand, is plagued by inhomogeneous deposition of Li metal, with the generation of voids and pits on the surface. Based on the comprehensive set of electrochemical and morphological data, the *l*-DES10 formulation was identified as the superior electrolyte chemistry, offering enhanced lithium cycling stability, lower interfacial resistance and more uniform lithium deposition.

In conclusion, while the obtained results leave room to improvement, the addition of the carbonates solution to the proposed DES has been shown to greatly enhance the electrochemical performance and to enable stable cycling of *in-situ* deposited and crosslinked GPEs.

4. Conclusions

In this work, a novel DES-based gel polymer electrolyte was fabricated via a fast, cheap and environmentally friendly thiol-ene polymerization to evaluate their viability as electrolytes in LMBs. Half-cell production was carried out in a dry environment, employing a novel *in-situ* manufacturing process, without the need for a separator or support. The physico-chemical performances of the DES-based liquid electrolyte were evaluated via several characterization methods, multinuclear NMR, FTIR-ATR and Raman spectroscopic analysis. The addition of 10 *wt%* EDL solution (EC/DEC, 1:1 *wt*) to the *l*-DES results in lower viscosity and a more dynamic Li^+ solvation shell, leading to superior ionic conductivity and transport properties with the increase of Li^+ conductivity from 4.13×10^{-4} S cm^{-1} for *g*-DES to 8.37×10^{-4} S cm^{-1} for *g*-DES10 at 20 °C. Moreover, it was shown that the EDL addition was beneficial with respect to Li morphology on the anode surface, where a smoother and more homogeneous surface was observed. The GPEs, obtained by crosslinking PEGDA and T4 in the liquid electrolyte solutions, retained good electrochemical performances and non-flammability, while improving the mechanical stability and the cell safety. Moreover, the EDL addition was associated with a significant increase in cell lifetime, resulting in the *g*-DES10 stable cycling for 113 cycles with a specific capacity of 163 mAh g^{-1}.

In summary, this work highlights the potential of DES-based systems as safe, high-performance electrolytes for next-generation lithium metal batteries. The *in-situ* production process can be considered as a suitable and compelling strategy for the development of easily up-scalable GPEs

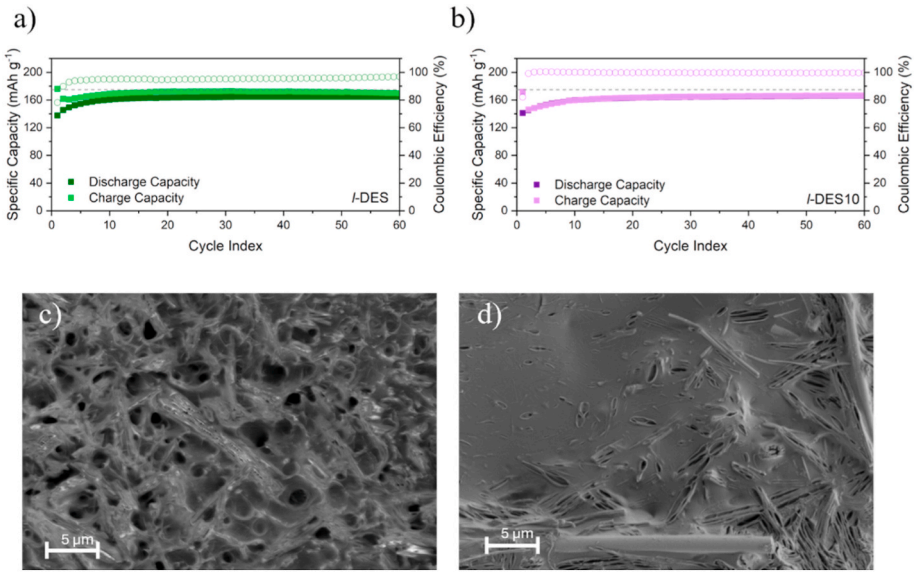


Fig. 5. Specific capacity and Coulombic efficiency of (a) *l*-DES and (b) *l*-DES10 during galvanostatic cycling. Li surface micrographs of (c) *l*-DES and (d) *l*-DES10-containing cells after galvanostatic cycling.

for future Li metal batteries.

CRediT authorship contribution statement

Mattia Longo: Writing – original draft, Methodology, Investigation, Conceptualization. **Matteo Gandolfo:** Methodology, Conceptualization. **Francesco Schimmenti:** Methodology, Conceptualization. **Javier Rodriguez del Real:** Methodology, Conceptualization. **Leire Meabe:** Writing – review & editing, Methodology, Conceptualization. **Maria Martinez Ibañez:** Writing – review & editing. **Daniela Fontana:** Writing – review & editing. **Julia Amici:** Writing – review & editing, Supervision, Methodology.

Declaration of competing interest

The authors declare that they have no known competing financial interests or personal relationships that could have appeared to influence the work reported in this paper.

Acknowledgments

The authors want to thank Dr. Mattia Spedicati for the opportunity to perform mechanical testing. This publication is part of the project PNRR-NGEU, which has received funding from the MUR–DM 352/2022.

Appendix A. Supplementary data

Supplementary data related to this article can be found online at https://doi.org/10.1016/j.jpowsour.2026.239709

Data availability

Data will be made available on request.

References

[1] H. Niu, N. Zhang, Y. Lu, Z. Zhang, M. Li, J. Liu, N. Zhang, W. Song, Y. Zhao, Z. Miao, Strategies toward the development of high-energy-density lithium batteries, J. Energy Storage 88 (2024) 111666, https://doi.org/10.1016/j.est.2024.111666.

[2] X. Yang, K.R. Adair, X. Gao, X. Sun, Recent advances and perspectives on thin electrolytes for high-energy-density solid-state lithium batteries, Energy Environ. Sci. 14 (2021) 643–671, https://doi.org/10.1039/D0EE02714F.

[3] B. Zhu, X. Wang, P. Yao, J. Li, J. Zhu, Towards high energy density lithium battery anodes: silicon and lithium, Chem. Sci. 10 (2019) 7132–7148, https://doi.org/10.1039/C9SC01201J.

[4] X. Ren, L. Zou, X. Cao, M.H. Engelhard, W. Liu, S.D. Burton, H. Lee, C. Niu, B. E. Matthews, Z. Zhu, C. Wang, B.W. Arey, J. Xiao, J. Liu, J.-G. Zhang, W. Xu, Enabling high-voltage lithium-metal batteries under practical conditions, Joule 3 (2019) 1662–1676, https://doi.org/10.1016/j.joule.2019.05.006.

[5] N. Piao, J. Wang, X. Gao, R. Li, H. Zhang, G. Hu, Z. Sun, X. Fan, H.-M. Cheng, F. Li, Designing temperature-insensitive solvated electrolytes for low-temperature lithium metal batteries, J. Am. Chem. Soc. 146 (2024) 18281–18291, https://doi.org/10.1021/jacs.4c01735.

[6] Y. Huang, H. Yang, Y. Gao, G. Chen, Y. Li, L. Shi, D. Zhang, Mechanism and solutions of lithium dendrite growth in lithium metal batteries, Mater. Chem. Front. 8 (2024) 1282–1299, https://doi.org/10.1039/D3QM01151H.

[7] J. Wang, B. Ge, H. Li, M. Yang, J. Wang, D. Liu, C. Fernandez, X. Chen, Q. Peng, Challenges and progresses of lithium-metal batteries, Chem. Eng. J. 420 (2021) 129739, https://doi.org/10.1016/j.cej.2021.129739.

[8] S. Gao, F. Sun, N. Liu, H. Yang, P.-F. Cao, Ionic conductive polymers as artificial solid electrolyte interphase films in Li metal batteries – a review, Mater. Today 40 (2020) 140–159, https://doi.org/10.1016/j.mattod.2020.06.011.

[9] Y. Xu, K. Dong, Y. Jie, P. Adelhelm, Y. Chen, L. Xu, P. Yu, J. Kim, Z. Kochovski, Z. Yu, W. Li, J. LeBeau, Y. Shao-Horn, R. Cao, S. Jiao, T. Cheng, I. Manke, Y. Lu, Promoting mechanistic understanding of lithium deposition and solid-electrolyte interphase (SEI) formation using advanced characterization and simulation methods: recent progress, limitations, and future perspectives, Adv. Energy Mater. 12 (2022), https://doi.org/10.1002/aenm.202200398.

[10] R. Wang, W. Cui, F. Chu, F. Wu, Lithium metal anodes: present and future, J. Energy Chem. 48 (2020) 145–159, https://doi.org/10.1016/j.jechem.2019.12.024.

[11] C. Fang, X. Wang, Y.S. Meng, Key issues hindering a practical lithium-metal anode, Trends Chem. 1 (2019) 152–158, https://doi.org/10.1016/j.trechm.2019.02.015.

[12] S. Xia, X. Wu, Z. Zhang, Y. Cui, W. Liu, Practical challenges and future perspectives of all-solid-state lithium-metal batteries, Chem 5 (2019) 753–785, https://doi.org/10.1016/j.chempr.2018.11.013.

[13] T. Krauskopf, F.H. Richter, W.G. Zeier, J. Janek, Physicochemical concepts of the lithium metal anode in solid-state batteries, Chem. Rev. 120 (2020) 7745–7794, https://doi.org/10.1021/acs.chemrev.0c00431.

[14] C. Ma, W. Cui, X. Liu, Y. Ding, Y. Wang, In situ preparation of gel polymer electrolyte for lithium batteries: progress and perspectives, InfoMat 4 (2022), https://doi.org/10.1002/inf2.12232.

[15] W. Chae, B. Kim, W.S. Ryoo, T. Earmme, A brief review of gel polymer electrolytes using in situ polymerization for lithium-ion polymer batteries, Polymers 15 (2023) 803, https://doi.org/10.3390/polym15040803.

[16] K. Zhou, X. Dai, P. Li, L. Zhang, X. Zhang, C. Wang, J. Wen, G. Huang, S. Xu, Recent advances in deep eutectic solvents for next-generation lithium batteries: safer and greener, Prog. Mater. Sci. 146 (2024) 101338, https://doi.org/10.1016/j.pmatsci.2024.101338.

[17] E.L. Smith, A.P. Abbott, K.S. Ryder, Deep eutectic solvents (DESs) and their applications, Chem. Rev. 114 (2014) 11060–11082, https://doi.org/10.1021/cr300162p.

[18] H. Niu, L. Wang, P. Guan, N. Zhang, C. Yan, M. Ding, X. Guo, T. Huang, X. Hu, Recent advances in application of ionic liquids in electrolyte of lithium ion batteries, J. Energy Storage 40 (2021) 102659, https://doi.org/10.1016/j.est.2021.102659.

[19] A. Sharma, R. Sharma, R.C. Thakur, L. Singh, An overview of deep eutectic solvents: alternative for organic electrolytes, aqueous systems & ionic liquids for electrochemical energy storage, J. Energy Chem. 82 (2023) 592–626, https://doi.org/10.1016/j.jechem.2023.03.039.
[20] R. Puttaswamy, C. Mondal, D. Mondal, D. Ghosh, An account on the deep eutectic solvents-based electrolytes for rechargeable batteries and supercapacitors, Sustain. Mater. Technol. 33 (2022) e00477, https://doi.org/10.1016/j.susmat.2022.e00477.
[21] A. Boisset, S. Menne, J. Jacquemin, A. Balducci, M. Anouti, Deep eutectic solvents based on N-methylacetamide and a lithium salt as suitable electrolytes for lithium-ion batteries, Phys. Chem. Chem. Phys. 15 (2013) 20054, https://doi.org/10.1039/c3cp53406e.
[22] Q. Li, Z. Zhang, Y. Li, H. Li, Z. Liu, X. Liu, Q. Xu, Rapid self-healing gel electrolyte based on deep eutectic solvents for solid-state lithium batteries, ACS Appl. Mater. Interfaces 14 (2022) 49700–49708, https://doi.org/10.1021/acsami.2c12445.
[23] W. Ye, J. Wang, C. Zhang, Z. Xue, Eutectic solution enables powerful click reaction for in-situ construction of advanced gel electrolytes, Energy Environ. Mater. 6 (2023), https://doi.org/10.1002/eem2.12579.
[24] X. Pei, Y. Li, T. Ou, X. Liang, Y. Yang, E. Jia, Y. Tan, S. Guo, Li−N interaction induced deep eutectic gel polymer electrolyte for high performance lithium-metal batteries, Angew. Chem. Int. Ed. 61 (2022), https://doi.org/10.1002/anie.202205075.
[25] M. Longo, M. Gandolfo, N.A. Plebani, C.A. Calderon, M. Destro, D. Fontana, S. Bodoardo, J. Amici, Comparative study of photopolymerized gel polymer electrolytes obtained via thiol-ene click reaction for Li metal batteries, Energy Environ. Mater. (2025), https://doi.org/10.1002/eem2.70028.
[26] T.T.A. Dinh, T.T.K. Huynh, L.T.M. Le, T.T.T. Truong, O.H. Nguyen, K.T.T. Tran, M. V. Tran, P.H. Tran, W. Kaveevivitchai, P.M.L. Le, Deep eutectic solvent based on lithium bis[(trifluoromethyl)sulfonyl] imide (LiTFSI) and 2,2,2-Trifluoroacetamide (TFA) as a promising electrolyte for a high voltage lithium-ion battery with a $LiMn_2O_4$ cathode, ACS Omega 5 (2020) 23843–23853, https://doi.org/10.1021/acsomega.0c03099.
[27] A.R. Harifi-Mood, F. Sharifi, H.R. Bijanzadeh, ^{23}Na-NMR data based donor number and their correlation with solvatochromic parameters in binary solvent mixtures, ChemistrySelect 6 (2021) 600–608, https://doi.org/10.1002/slct.202003441.
[28] C.M. Burke, V. Pande, A. Khetan, V. Viswanathan, B.D. McCloskey, Enhancing electrochemical intermediate solvation through electrolyte anion selection to increase nonaqueous Li–O_2 battery capacity, Proc. Natl. Acad. Sci. 112 (2015) 9293–9298, https://doi.org/10.1073/pnas.1505728112.
[29] J. Evans, C.A. Vincent, P.G. Bruce, Electrochemical measurement of transference numbers in polymer electrolytes, Polymer (Guildf.) 28 (1987) 2324–2328, https://doi.org/10.1016/0032-3861(87)90394-6.
[30] S. Spittle, I. Alfurayj, B.B. Hansen, K. Glynn, W. Brackett, R. Pandian, C. Burda, J. Sangoro, Enhanced dynamics and charge transport at the eutectic point: a new paradigm for the use of deep eutectic solvent systems, JACS Au 3 (2023) 3024–3030, https://doi.org/10.1021/jacsau.3c00420.
[31] X. Zhao, Z. Fu, X. Zhang, X. Wang, B. Li, D. Zhou, F. Kang, More is better: high-entropy electrolyte design in rechargeable batteries, Energy Environ. Sci. 17 (2024) 2406–2430, https://doi.org/10.1039/D3EE03821A.
[32] Z. Lu, L. Yang, Y. Guo, Thermal behavior and decomposition kinetics of six electrolyte salts by thermal analysis, J. Power Sources 156 (2006) 555–559, https://doi.org/10.1016/j.jpowsour.2005.05.085.
[33] Y.-Y. Di, Z.-C. Tan, X.-M. Wu, S.-H. Meng, S.-S. Qu, Heat capacity and thermochemical study of trifluoroacetamide (C2H2F3NO), Thermochim. Acta 356 (2000) 143–151, https://doi.org/10.1016/S0040-6031(00)00479-2.
[34] H. Ogawa, H. Mori, Lithium salt/amide-based deep eutectic electrolytes for lithium-ion batteries: electrochemical, thermal and computational study, Phys. Chem. Chem. Phys. 22 (2020) 8853–8863, https://doi.org/10.1039/D0CP01255F.
[35] T. Forsting, H.C. Gottschalk, B. Hartwig, M. Mons, M.A. Suhm, Correcting the record: the dimers and trimers of trans-N-methylacetamide, Phys. Chem. Chem. Phys. 19 (2017) 10727–10737, https://doi.org/10.1039/C6CP07989J.
[36] H. Abdelmoulahi, H. Ghalla, S.A. Brandán, S. Nasr, H. Abdelmoulahi, H. Ghalla, S. A. Brandán, S. Nasr, Structural study and vibrational analyses of the monomeric, dimeric, trimeric and tetrameric species of acetamide by using the FT-IR and Raman spectra, DFT calculations and SQM met structural study and vibrational analyses of the monomeric, dimeric, trimeric and tetrameric species of acetamide by using the FT-IR and Raman spectra, DFT calculations and SQM methodology, J. Mater. Environ. Sci. 6 (2015) 3094–3109. https://www.researchgate.net/publication/285482938.
[37] I.T. Rakipov, A.A. Petrov, A.A. Akhmadiyarov, A.A. Khachatrian, M. A. Varfolomeev, FTIR spectral study of intermolecular interactions of C=O groups of amides in solution, J. Mol. Liq. 354 (2022) 118838, https://doi.org/10.1016/j.molliq.2022.118838.
[38] H.I. Okur, J. Kherb, P.S. Cremer, Cations bind only weakly to amides in aqueous solutions, J. Am. Chem. Soc. 135 (2013) 5062–5067, https://doi.org/10.1021/ja3119256.
[39] G. Zhang, W. Wang, D. Chen, Chemical origin of red shift of CO stretching vibration in acetone complexes with various metal cations, Chem. Phys. 359 (2009) 40–44, https://doi.org/10.1016/j.chemphys.2009.03.004.
[40] Y. Hu, Z. Wang, H. Li, X. Huang, L. Chen, Spectroscopic and DFT studies to understand the liquid formation mechanism in the LiTFSI/acetamide complex system, Spectrochim. Acta Mol. Biomol. Spectrosc. 61 (2005) 2009–2015, https://doi.org/10.1016/j.saa.2004.07.032.
[41] Y. Liu, Z. Wang, J. Wang, K. Tian, X. Meng, G. Mao, Investigation on binding between cations and amides using UV Raman spectroscopy, Chin. J. Chem. Phys. 37 (2024) 539–544, https://doi.org/10.1063/1674-0068/cjcp2301008.
[42] U. Kulkarni, W. Cho, S. Lee, D.S. Hwang, T. Im, Y.K. Jeong, K. Ahn, G.-R. Yi, Donor numbers for ionic liquids and carbonate solvents using 7Li and 23Na as probes, Kor. J. Chem. Eng. 42 (2025) 225–231, https://doi.org/10.1007/s11814-024-00356-2.
[43] S. Sekhon, Effect of donor number of solvent on the conductivity behaviour of nonaqueous proton-conducting polymer gel electrolytes, Solid State Ionics 160 (2003) 301–307, https://doi.org/10.1016/S0167-2738(03)00167-X.
[44] Q. You, Y. Sun, F. Wang, J. Cheng, F. Tang, Decoding the competing effects of dynamic solvation structures on nuclear magnetic resonance chemical shifts of battery electrolytes via machine learning, J. Am. Chem. Soc. 147 (2025) 14667–14676, https://doi.org/10.1021/jacs.5c02710.
[45] S.K. Patla, A. Roy Choudhury, R. Ray, S. Das, S. Karmakar, Plasticizer ethylene carbonate facilitates new ion coordination site in blend polymer electrolyte: dielectric relaxation through two-parameter Mittag-Leffler function, AIP Adv. 10 (2020), https://doi.org/10.1063/5.0018380.
[46] D.M. Seo, S. Reininger, M. Kutcher, K. Redmond, W.B. Euler, B.L. Lucht, Role of mixed solvation and ion pairing in the solution structure of lithium ion battery electrolytes, J. Phys. Chem. C 119 (2015) 14038–14046, https://doi.org/10.1021/acs.jpcc.5b03694.
[47] P. Wróbel, P. Kubisiak, A. Eilmes, MeTFSI (Me = Li, Na) solvation in ethylene carbonate and fluorinated ethylene carbonate: a molecular dynamics study, J. Phys. Chem. B 125 (2021) 1248–1258, https://doi.org/10.1021/acs.jpcb.0c10622.
[48] S.-A. Hyodo, K. Okabayashi, Raman intensity study of local structure in non-aqueous electrolyte solutions—I. Cation-solvent interaction in LiClO4/ethylene carbonate, Electrochim. Acta 34 (1989) 1551–1556, https://doi.org/10.1016/0013-4686(89)87040-9.
[49] D.M. Seo, P.D. Boyle, R.D. Sommer, J.S. Daubert, O. Borodin, W.A. Henderson, Solvate structures and spectroscopic characterization of LiTFSI electrolytes, J. Phys. Chem. B 118 (2014) 13601–13608, https://doi.org/10.1021/jp505006x.
[50] D. Brouillette, D.E. Irish, N.J. Taylor, G. Perron, M. Odziemkowski, J.E. Desnoyers, Stable solvates in solution of lithium bis(trifluoromethylsulfone)imide in glymes and other aprotic solvents: phase diagrams, crystallography and Raman spectroscopyElectronic supplementary information (ESI) available: crystallographic data (single crystal data) in cif format (CCDC reference number 184345), Phys. Chem. Chem. Phys. 4 (2002) 6063–6071, https://doi.org/10.1039/b203776a. See, http://www.rsc.org/suppdata/cp/b2/b203776a/.
[51] Q. Pang, A. Shyamsunder, B. Narayanan, C.Y. Kwok, L.A. Curtiss, L.F. Nazar, Tuning the electrolyte network structure to invoke quasi-solid state sulfur conversion and suppress lithium dendrite formation in Li–S batteries, Nat. Energy 3 (2018) 783–791, https://doi.org/10.1038/s41560-018-0214-0.
[52] W. Linert, A. Camard, M. Armand, C. Michot, Anions of low Lewis basicity for ionic solid state electrolytes, Coord. Chem. Rev. 226 (2002) 137–141, https://doi.org/10.1016/S0010-8545(01)00416-7.
[53] Z. Lu, L. Peng, Y. Rong, E. Wang, R. Shi, H. Yang, Y. Xu, R. Yang, C. Jin, Enhanced electrochemical properties and optimized Li^+ transmission pathways of <scp>PEO</scp>/<scp>LLZTO</scp> -based composite electrolytes modified by supramolecular combination, Energy Environ. Mater. 7 (2024), https://doi.org/10.1002/eem2.12498.
[54] B.A. Fortuin, J. Otegi, J.M. López del Amo, S.R. Peña, L. Meabe, H. Manzano, M. Martínez-Ibañez, J. Carrasco, Synergistic theoretical and experimental study on the ion dynamics of bis(trifluoromethanesulfonyl)imide-based alkali metal salts for solid polymer electrolytes, Phys. Chem. Chem. Phys. 25 (2023) 25038–25054, https://doi.org/10.1039/D3CP02989A.
[55] B.A. Fortuin, L. Meabe, S.R. Peña, Y. Zhang, L. Qiao, J. Etxabe, L. Garcia, H. Manzano, M. Armand, M. Martínez-Ibañez, J. Carrasco, Molecular-level insight into charge carrier transport and speciation in solid polymer electrolytes by chemically tuning both polymer and lithium salt, J. Phys. Chem. C 127 (2023) 1955–1964, https://doi.org/10.1021/acs.jpcc.2c07032.
[56] M.C. Burroughs, T.H. Schloemer, D.N. Congreve, D.J. Mai, Gelation dynamics during photo-cross-linking of polymer nanocomposite hydrogels, ACS Polymers Au 3 (2023) 217–227, https://doi.org/10.1021/acspolymersau.2c00051.
[57] J. Tang, X. Duan, Q. Chen, Temperature dependence of the gel modulus depends on change of solvent quality, Macromolecules 56 (2023) 8574–8580, https://doi.org/10.1021/acs.macromol.3c01671.
[58] W. Weng, Z. Li, A.M. Jamieson, S.J. Rowan, Control of gel morphology and properties of a class of metallo-supramolecular polymers by good/poor solvent environments, Macromolecules 42 (2009) 236–246, https://doi.org/10.1021/ma801046w.
[59] S.H. Gwon, J. Yoon, H.K. Seok, K.H. Oh, J.-Y. Sun, Gelation dynamics of ionically crosslinked alginate gel with various cations, Macromol. Res. 23 (2015) 1112–1116, https://doi.org/10.1007/s13233-015-3151-9.
[60] V. Javvaji, A.G. Baradwaj, G.F. Payne, S.R. Raghavan, Light-activated ionic gelation of common biopolymers, Langmuir 27 (2011) 12591–12596, https://doi.org/10.1021/la201860s.
[61] V. Jabbari, V. Yurkiv, M.G. Rasul, M.T. Saray, R. Rojaee, F. Mashayek, R. Shahbazian-Yassar, An efficient gel polymer electrolyte for dendrite-free and long cycle life lithium metal batteries, Energy Storage Mater. 46 (2022) 352–365, https://doi.org/10.1016/j.ensm.2022.01.031.
[62] Q. Li, B. Quan, W. Li, J. Lu, J. Zheng, X. Yu, J. Li, H. Li, Electro-plating and stripping behavior on lithium metal electrode with ordered three-dimensional structure, Nano Energy 45 (2018) 463–470, https://doi.org/10.1016/j.nanoen.2018.01.019.
[63] H. Liang, H. Li, Z. Wang, F. Wu, L. Chen, X. Huang, New binary room-temperature molten salt electrolyte based on urea and LiTFSI, J. Phys. Chem. B 105 (2001) 9966–9969, https://doi.org/10.1021/jp0119779.

[64] C. Zhang, L. Zhang, G. Yu, Eutectic electrolytes as a promising platform for next-generation electrochemical energy storage, Acc. Chem. Res. 53 (2020) 1648–1659, https://doi.org/10.1021/acs.accounts.0c00360.
[65] Y. Li, F. Lian, L. Ma, C. Liu, L. Yang, X. Sun, K. Chou, Fluoroethylene carbonate as electrolyte additive for improving the electrochemical performances of high-capacity Li1.16[Mn0.75Ni0.25]0.84O2 material, Electrochim. Acta 168 (2015) 261–270, https://doi.org/10.1016/j.electacta.2015.04.030.
[66] M.Z. Kufian, S.R. Majid, Performance of lithium-ion cells using 1 M LiPF6 in EC/DEC (v/v = 1/2) electrolyte with ethyl propionate additive, Ionics 16 (2010) 409–416, https://doi.org/10.1007/s11581-009-0413-6.